Smart Structures and Systems, *Vol. 32, No. 5 (2023) 281-295*
https://doi.org/10.12989/sss.2023.32.5.281

Modeling and experimental verification of phase-control active tuned mass dampers applied to MDOF structures

Yong-An Lai*, Pei-Tzu Chang [a] and Yan-Liang Kuo [b]

Department of Civil Engineering, National Central University, No. 300, Zhongda Rd., Zhongli District, Taoyuan City 320317, Taiwan (R.O.C.)

(*Received June 30, 2023, Revised October 8, 2023, Accepted October 15, 2023*)

Abstract. The purpose of this study is to demonstrate and verify the application of phase-control absolute-acceleration-feedback active tuned mass dampers (PCA-ATMD) to multiple-degree-of-freedom (MDOF) building structures. In addition, servo speed control technique has been developed as a replacement for force control in order to mitigate the negative effects caused by friction and inertia. The essence of the proposed PCA-ATMD is to achieve a 90° phase lag for a structure by implementing the desired control force so that the PCA-ATMD can receive the maximum power flow with which to effectively mitigate the structural vibration. An MDOF building structure with a PCA-ATMD and a real-time filter forming a complete system is modeled using a state-space representation and is presented in detail. The feedback measurement for the phase control algorithm of the MDOF structure is compact, with only the absolute acceleration of one structural floor and ATMD's velocity relative to the structure required. A discrete-time direct output-feedback optimization method is introduced to the PCA-ATMD to ensure that the control system is optimized and stable. Numerical simulation and shaking table experiments are conducted on a three-story steel shear building structure to verify the performance of the PCA-ATMD. The results indicate that the absolute acceleration of the structure is well suppressed whether considering peak or root-mean-square responses. The experiment also demonstrates that the control of the PCA-ATMD can be decentralized, so that it is convenient to apply and maintain to real high-rise building structures.

Keywords: active tuned mass damper; discrete-time direct output feedback; multi-degree-of-freedom building structure; phase control; seismic excitation; servo-velocity control; shaking table experiment

1. Introduction

A conventional passive tuned mass damper (PTMD) is a passive structural control device composed of a mass, spring, and dashpot. Since the concept of using a mass–spring system was proposed by Frahm (1911) for vibration mitigation, Den Hartog (1956), Ayorinde and Warburton (1980), Warburton (1982), Tsai and Lin (1993), Sadek *et al*. (1997), Bakre and Jangid (2007), Tigli (2012), and many other scholars (Ghosh and Basu 2005, Chu *et al*. 2005, Aydin *et al*. 2019) have developed the optimization theory and design method of PTMDs. Over the past few decades, PTMDs have been employed for structural vibration reduction in high-rise buildings worldwide, such as in Taipei 101 and Taipei Nanshan Plaza in Taipei, Shanghai Tower in Shanghai, the Shinjuku Nomura Building and Tokyo Skytree in Tokyo, Almas Tower in Dubai, Steinway Tower and 432 Park Avenue in New York, and One Barangaroo in Sydney (Gutierrez Soto and Adeli 2013, Soong and Dargush 1997, Nagarajaiah 2009, Lago *et al*. 2018). Because the effect of PTMDs on seismic response mitigation depends on the frequency content, frequency bandwidth, and duration of the strong motion (Pinkaew *et al*. 2003, Murudi and Mane 2004, Dai *et al*. 2020), the performance of PTMDs at mitigating earthquake-induced damage varies widely. Therefore, the function of the PTMDs installed in the high-rise buildings of the world is primarily to resist wind disturbances. Utilization of PTMDs to resist earthquakes efficiently is still rare and under development (Sone *et al*. 2019).

In the research and practice of active control theory of building structures for disturbance rejection, the effects of active control for structures have been widely recognized through theoretical derivation, numerical simulation, experimental validation, and field testing (Soong and Manolis 1987, Chung *et al*. 1989, Spencer *et al*. 1994). One of the most attractive applications in civil and mechanical engineering is the use of active tuned mass dampers (ATMD) or active mass dampers/drivers (AMD). Since Chang and Soong (1980) first numerically studied the feasibility of active control via TMD application, various optimal ATMD control theories and studies of single-degree-of-freedom (SDOF) structures have been conducted (Nishimura *et al*. 1992, Chang and Yang 1995, Nagishima 2001).

Although it is generally recognized that ATMDs outperform PTMDs, implementing ATMDs to control multiple-degree-of-freedom (MDOF) building structures is much more difficult than for SDOF structures. A major difficulty is that the states of MDOF building structures are

*Corresponding author, Ph.D., Assistant Professor,
E-mail: laiyongan@ncu.edu.tw
[a] M.S.
[b] M.S.

ISSN: 1738-1584 (Print), 1738-1991 (Online)

not readily available, with usually only a few measurements assessable in the field. Spencer *et al*. (1998) experimentally studied a three-floor benchmark structure with a hydraulic-driven active mass driver installed and showed some of the ATMD design and implementation challenges such available measurements. Loh and Chao (1996) compared the effectiveness of PTMDs and ATMDs in MDOF structure and proposed a systematic design method for the quadratic weighting matrix of linear quadratic regulator (LQR) control to achieve desired performance. Rasouli and Yahyai (2002) compared the control effects of implementing PTMD and ATMD on a 25-story building during the El Centro and Tabas earthquakes, and the results showed that an ATMD is superior to a PTMD in high-rise buildings during earthquakes. Li *et al*. (Li and Liu 2002, Li *et al*. 2003) conducted a series of studies on the damping of base vibration achieved by active multiple tuned mass dampers (MATMD), showing that the AMTMD is more effective and convenient to implement compared to one massive ATMD. Because fuzzy logic controller exhibits great potential in active control, Guclu and Yazici (2008) compared the performance of fuzzy control and the proportional-derivative (PD) control law for ATMD to suppress earthquake forces. Yang *et al*. (2017) proposed a negative-acceleration-feedback control algorithm to calculate the desired displacement for the ATMD in order to effectively increase the model damping of the MDOF structure. Allaoua and Guenfaf (2019) demonstrated the influence of soil–structure interaction (SSI) on the effectiveness of the ATMD in vibration control, and the results showed that it is important to consider SSI when a structure is on soft soil. Concha *et al*. (2021) proposed an automatic tuning algorithm for a sliding mode controller (SMC) based on Ackermann's formula. Their experimental results showed that the automatically tuned SMC yields superior performance and robustness compared to traditional LQR in the MDOF structure. Chen *et al*. (2021) utilized the symbiotic organisms search technique for a LQR-controlled active mass damper (AMD) system. This approach allows for the optimization of the LQR weighting matrices, thereby enhancing the performance of AMD system.

Numerous articles have been written about MDOF structures installed with ATMD (Yang 1987, Samali and Al-Dawod 2003, Spencer and Nagarajaiah 2003, Mitchell *et al*. 2012, Saaed *et al*. 2013, Younesoiur and Ghaffarzadeh 2015, Paul and Yu 2018), discussing the performance of ATMD under different base excitations, limited control authority, computational delay, and using different control laws. Most of previously mentioned research reported that ATMDs outperform PTMDs and are more feasible in resisting earthquakes. Currently, ATMDs are mainly implemented in practical applications in Japan, such as in the Kyobashi Seiwa Building, Sendagaya INTES Building, and Riverside Sumida Central Tower in Tokyo, as well as in the Hankyu Chayamachi Building and Herbis Osaka in Osaka (Kareem *et al*. 1999, Ikeda 2009, Casciati *et al*. 2012).

Since the proposal of power flow theory by Soong and Dargush (Soong and Dargush 1997), which revealed that the passive TMD yields the best performance when it has a 90° phase lag relative to the primary structure, the concept of phase control as applied to SATMD systems has been studied by Chung *et al*. (2013), Moutinho (2015), Ferreira *et al*. (2018), Lai *et al*. (2018), and Amini *et al*. (2018). Recently, Lai *et al*. (2022) demonstrated the phase control of an ATMD system for a SDOF building is feasible. Their work showed that the proposed phase control algorithm only requires two measurements: one is the ATMD's relative velocity and another one is structural absolute acceleration. However, the feasibility of applying a phase-control ATMD system to an MDOF building structure only using these limited measurements to control a whole MODF building is still waiting to be answered. The primary issue arises when an accelerometer is installed on a MDOF building structure. The accelerometer not only captures the fundamental modal responses but also records other higher modal responses during earthquakes. The influence of these recorded higher modal accelerations on the control algorithm remain unclear. Moreover, measuring only the acceleration of the floor where the ATMD is installed may be convenient for practical application, but whether it is sufficient for controlling the entire building structure requires further in-depth discussion. These measurement issues differ significantly from the case of a SDOF structure and necessitate additional numerical studies and experimental verification.

In this paper, the performance of an MDOF structure implemented with a PCA-ATMD is verified through numerical simulation and a shaking table experiment. A servo-velocity control technique is also developed for the ATMD system for practical application. The proposed phase control algorithm of the PCA-ATMD is smooth and proportional, and neither full-state system measurement nor estimation are required. The control object is an MDOF building and the only measurements needed for the PCA-ATMD are the velocity of the ATMD relative to the structure and the absolute acceleration of the structural floor on which the PCA-ATMD is located. These two measurements can be acquired from one building floor, enabling the PCA-ATMD to be operated in a decentralized manner. The dynamics of the MDOF building structure implemented with the ATMD system and the digital filter are comprehensively introduced and derived in a single state-space model, so that the phase control gains can be optimized precisely through the direct output-feedback method. In this way, the stability of the proposed control algorithm and framework can be ensured. A three-floor building structure with a PCA-ATMD is subjected to earthquake forces to verify the effectiveness of its structural vibration mitigation. Additionally, a servo-velocity control technique is applied to mitigate the loss of active control power caused by common friction and inertia. This is achieved by converting the structural disturbance rejection problem into a reference tracking problem by the proposed velocity predictor.

2. Problem formulation

2.1 Modeling of a physical MDOF structure implemented with an ATMD

As shown in Fig. 1(a), the equation of motion of an N-floor shear building structure subjected to base excitation is

$$\boldsymbol{m}_s\ddot{\boldsymbol{x}}_s(t) + \boldsymbol{c}_s\dot{\boldsymbol{x}}_s(t) + \boldsymbol{k}_s\boldsymbol{x}_s(t) = -\boldsymbol{m}_s\mathbf{1}\ddot{x}_g(t) \tag{1}$$

where $\boldsymbol{x}_s(t) = [x_N(t) \quad \cdots \quad x_1(t)]^T$ is the displacement vector, $x_i(t), i = 1, \cdots, N$ is the floor displacement relative to the base, and the superscript T denotes the matrix transpose; $\mathbf{m}_s$ is the structural mass matrix; $\mathbf{c}_s$ is the damping matrix; $\mathbf{k}_s$ is the stiffness matrix; $\mathbf{1}$ is a column vector with each element equal to unity; and $\ddot{x}_g(t)$ is the base acceleration.

For an ATMD mounted at the j^{th}-floor of the shear building structure, as shown in Fig. 1(b), the system becomes an $N + 1$ degree-of-freedom system. The equation of motion of the augmented system is thus

$$\boldsymbol{M}_s\ddot{\boldsymbol{x}}(t) + \boldsymbol{C}_s\dot{\boldsymbol{x}}(t) + \boldsymbol{K}_s\boldsymbol{x}(t) = \boldsymbol{b}u(t) - \boldsymbol{M}_s\mathbf{1}\ddot{x}_g(t) \tag{2}$$

where $\boldsymbol{x}(t) = \begin{bmatrix} x_d(t) \\ \boldsymbol{x}_s(t) \end{bmatrix}$ is the displacement vector; $\boldsymbol{M}_s = m_i\boldsymbol{d}^T\boldsymbol{d} + \begin{bmatrix} m_d & \mathbf{0} \\ \mathbf{0} & \boldsymbol{m}_s \end{bmatrix}$ is the mass matrix, in which m_d and m_i are the mass and inertial mass of the ATMD, respectively, and the vector $\boldsymbol{d} = [1 \quad \mathbf{0}_{1\times(N-j)} \quad -1 \quad \mathbf{0}_{1\times(j-1)}]$ indicates the ATMD located on the j^{th}-floor; $\boldsymbol{C}_s = c_d\boldsymbol{d}^T\boldsymbol{d} + \begin{bmatrix} 0 & \mathbf{0} \\ \mathbf{0} & \boldsymbol{c}_s \end{bmatrix}$ is the damping matrix, in which c_d is the damping coefficient of the ATMD; $\boldsymbol{K}_s = k_d\boldsymbol{d}^T\boldsymbol{d} + \begin{bmatrix} 0 & \mathbf{0} \\ \mathbf{0} & \boldsymbol{k}_s \end{bmatrix}$ is the stiffness matrix, in which k_d is the stiffness of the ATMD; $\boldsymbol{b} = -\boldsymbol{d}^T$ is the active control force location vector; and $u(t)$ is the active control force.

Eq. (2) can be transformed into a first-order state-space equation as

$$\dot{\boldsymbol{z}}_s(t) = \boldsymbol{A}_s\boldsymbol{z}_s(t) + \boldsymbol{B}_su(t) + \boldsymbol{E}_s\ddot{x}_g(t) \tag{3}$$

where $\boldsymbol{z}_s(t) = \begin{bmatrix} \boldsymbol{x}(t) \\ \dot{\boldsymbol{x}}(t) \end{bmatrix}$ is the state vector of the system; $\boldsymbol{A}_s = \begin{bmatrix} \mathbf{0} & \boldsymbol{I} \\ -\boldsymbol{M}^{-1}\boldsymbol{K} & -\boldsymbol{M}^{-1}\boldsymbol{C} \end{bmatrix}$ is the system matrix; $\boldsymbol{B}_s = \begin{bmatrix} \mathbf{0} \\ \boldsymbol{M}^{-1}\boldsymbol{b} \end{bmatrix}$ is the state-space control force location vector; and $\boldsymbol{E}_s = \begin{bmatrix} \mathbf{0} \\ -\mathbf{1} \end{bmatrix}$ is the state-space external disturbance location vector.

If the sampling time, Δt, is sufficiently small, the base acceleration and the control force can be processed as a piecewise constant (zero-order hold) during the sampling time step. The discrete-time state-space equation can then be derived as

$$\boldsymbol{z}_s[k+1] = \boldsymbol{A}_d\boldsymbol{z}_s[k] + \boldsymbol{B}_du[k] + \boldsymbol{E}_d\ddot{x}_g[k] \tag{4}$$

where $\boldsymbol{A}_d = e^{\boldsymbol{A}\Delta t}$ is the discrete-time state-space system matrix and $\boldsymbol{B}_d = \boldsymbol{A}^{-1}(\boldsymbol{A}_d - \boldsymbol{I})\boldsymbol{B}$ and $\boldsymbol{E}_d = \boldsymbol{A}^{-1}(\boldsymbol{A}_d - \boldsymbol{I})\boldsymbol{E}$ are the discrete-time control force location vector and external excitation location vector, respectively.

From Eq. (3), the output of the absolute acceleration of the structural floor $y_{sa}[k]$ with respect to the system state $\mathbf{z}_s[k]$ can also be expressed as

$$y_{sa}[k] = \boldsymbol{C}_{sa}\boldsymbol{z}_s[k] + D_{sa}u[k] \tag{5}$$

where $\boldsymbol{C}_{sa} = \boldsymbol{d}_{sa}\boldsymbol{A}_s$, $D_{sa} = \boldsymbol{d}_{sa}\boldsymbol{B}_s$, and $\boldsymbol{d}_{sa} = [\mathbf{0}_{1\times(2N+2-j)} \quad 1 \quad \mathbf{0}_{1\times(j-1)}]$ is the vector to indicate corresponding structural floor.

2.2 Modeling of the digital filter in a state-space representation

For PCA-ATMD operation, an accelerometer is used to measure the absolute acceleration response of the floor on which the PCA-ATMD located. However, accelerometers are quite sensitive to environmental noise, which can result in undesired control effects and reduce the performance of the control system. Therefore, a digital filter is usually adopted for real-time filtering to remove noise. The Z-transform of a digital filter can be expressed as

$$H(z) = \frac{b_0 + b_1z^{-1} + b_2z^{-2} + \cdots + b_nz^{-n}}{a_0 + a_1z^{-1} + a_2z^{-2} + \cdots + a_nz^{-n}} \tag{6}$$

where b_n and a_n are the coefficients of the filter and n is the order of the filter. This nth-order digital filter transfer function can be realized by a single-in-single-out (SISO) discrete-time state-space representation

$$\boldsymbol{z}_f[k+1] = \boldsymbol{A}_f\boldsymbol{z}_f[k] + \boldsymbol{B}_fu_f[k] \tag{7a}$$

and

$$y_f[k] = \boldsymbol{C}_f\boldsymbol{z}_f[k] + D_fu_f[k] \tag{7b}$$

where $\mathbf{z}_f[k]$ is the state of the digital filter; $\boldsymbol{A}_f = \begin{bmatrix} -a_1 & -a_2 & \cdots & -a_n \\ 1 & & \mathbf{0} & 0 \\ & \ddots & & \vdots \\ \mathbf{0} & & 1 & 0 \end{bmatrix}$ and $\boldsymbol{B}_f = \begin{bmatrix} 1 \\ 0 \\ \vdots \\ 0 \end{bmatrix}$ are the system matrix and input vector of the filter; $u_f[k]$ is the input acceleration signal; $y_f[k]$ is the output signal; $\boldsymbol{C}_f = [b_1 \quad b_2 \quad \cdots \quad b_n]$ is the output vector; and $D_f = b_0$.

2.3 Modeling of the complete building–ATMD–digital filter combined system

The input signal for the applied digital filter is the absolute acceleration of structural floor, *i.e.*, $u_f[k] = y_{sa}[k]$. Therefore, substituting Eq. (5) into Eq. (7-1) yields

$$\boldsymbol{z}_f[k+1] = \boldsymbol{A}_f\boldsymbol{z}_f[k] + \boldsymbol{E}_f\boldsymbol{C}_s\boldsymbol{z}_s[k] + \boldsymbol{E}_fD_su[k] \tag{8}$$

Then the dynamics of the filter system, Eq. (8), and the building structure implemented with the ATMD system, Eq. (4), can be combined as

$$\boldsymbol{z}[k+1] = \boldsymbol{A}\boldsymbol{z}[k] + \boldsymbol{B}u[k] + \boldsymbol{E}\ddot{x}_g[k] \tag{9}$$

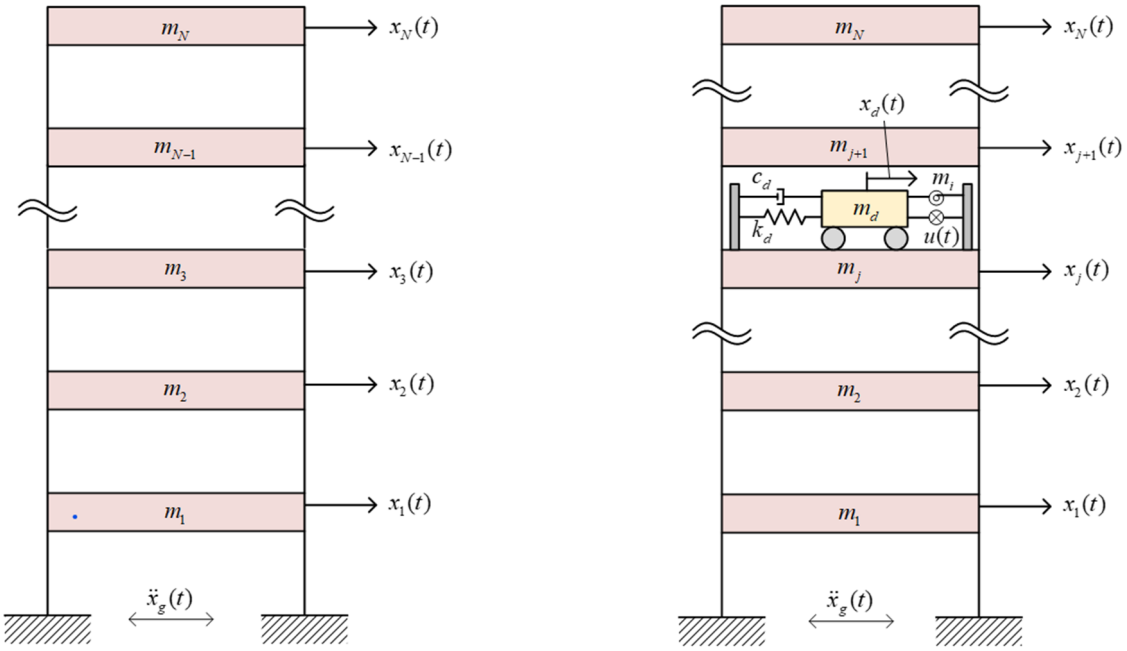

(a) MDOF building structure (b) MDOF structure implemented with an ATMD

Fig. 1 Schematics of a MDOF building structure with and without implemented with an ATMD

where $\boldsymbol{z}[k] = \begin{Bmatrix} \boldsymbol{z}_s[k] \\ \boldsymbol{z}_f[k] \end{Bmatrix}$ is the complete state that contains the physical building–ATMD system states and digital filter states; $\boldsymbol{A} = \begin{bmatrix} \boldsymbol{A}_d & \boldsymbol{0} \\ \boldsymbol{B}_f \boldsymbol{d}_{sa} \boldsymbol{A}_s & \boldsymbol{A}_f \end{bmatrix}$ is the complete system matrix; $\boldsymbol{B} = \begin{bmatrix} \boldsymbol{B}_d \\ \boldsymbol{B}_f \boldsymbol{d}_{sa} \boldsymbol{B}_s \end{bmatrix}$ is the complete control force vector; and $\boldsymbol{E} = \begin{bmatrix} \boldsymbol{E}_d \\ \boldsymbol{0} \end{bmatrix}$ is the complete excitation vector.

The filtered absolute acceleration of the structure of Eq. (7-2) can therefore be expressed as

$$y_f[k] = \boldsymbol{C}\boldsymbol{z}[k] + Du[k] \tag{10}$$

where $\boldsymbol{C} = [D_f \boldsymbol{d}_{sa} \boldsymbol{A}_s \quad C_f]$ and $D = D_f \boldsymbol{d}_{sa} \boldsymbol{B}_s$. Note that the term $\mathbf{d}_{sa}\mathbf{B}_s$ is a scalar of $\boldsymbol{d}_{sa}\boldsymbol{B}_s = \frac{m_d}{det(\boldsymbol{M})}$.

After applying the digital filter to the structural acceleration, the filtered signal will unavoidably contain some distortions, especially phase distortions and delay. These will significantly influence the control performance and stability. In view of this, stability can be ensured during the design process by using the complete model to design the control gains. It is worth remarking that, in this paper, the building–ATMD model and the digital filter are combined in the time domain by the state-space form rather than in the frequency domain. The advantage of combining these two dynamic systems in the time domain is that the physical meaning of the system states is known and determined. Thus, the system output and corresponding output vector are also easily determined for use in the optimal design process.

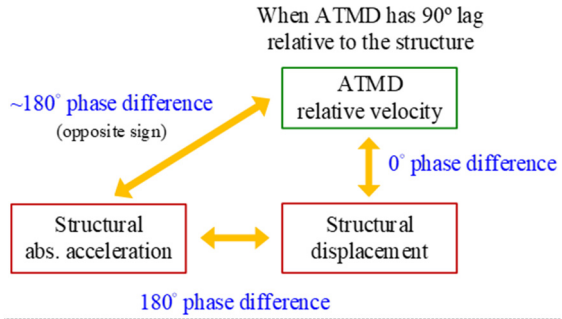

Fig. 2 Desired phase difference of the ATMD relative to the structure to achieve maximum power flow

3. Phase control algorithm for PCA-ATMD

A phase control strategy for a PCA-ATMD mounted in an SDOF structure was introduced in Lai *et al*. (2022). The main aim of control is to maintain the ATMD's 90° phase lag relative to the structure so that the ATMD has maximum power flow to achieve optimal performance (Soong and Dargush 1997). When this control is achieved, the ATMD's relative velocity will have a 0° phase lag relative to the structure. Furthermore, due to the fact that the displacement normally exhibits a 180° lag of the acceleration, the ATMD's relative velocity trajectory will also be the opposite sign of the structure's absolute acceleration after the amplitude is scaled by a factor. Thus, the control objective can then be transferred to minimize the trajectory difference of the ATMD's relative velocity and structural absolute acceleration as shown in Fig. 2.

For application of the PCA-ATMD to an MDOF structure, the trajectory error signal is therefore selected as

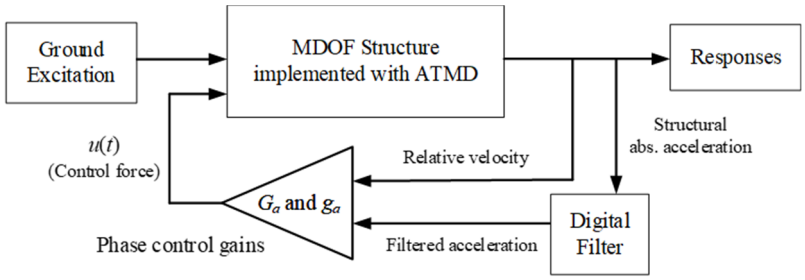

Fig. 3 Control flowchart for PCA-ATMD

$$\begin{aligned} e_a[k] &= (\dot{x}_d[k] - \dot{x}_j[k]) + g_a y_f[k] \\ &= \mathbf{d}_{rv}\mathbf{z}[k] + g_a y_f[k] \end{aligned} \tag{11}$$

where $e_a(t)$ is the TMD trajectory error regarding the ATMD's relative velocity $\dot{x}_d[k] - \dot{x}_j[k]$ and filtered absolute acceleration of structure $y_f[k]$ at the j^{th}-floor, as expressed in Eq. (10); g_a is the factor of the amplitude ratio that should be optimized; and $\boldsymbol{d}_{rv} = [\mathbf{0}_{1\times(N+1)} \quad \boldsymbol{d} \quad \mathbf{0}_{1\times n}]$ is the ATMD's relative-velocity output vector of the complete state such that $\mathbf{d}_{rv}\mathbf{z}[k]$ is the ATMD's velocity relative to the structure. It is worth remarking that Eq. (11) shows that the TMD trajectory error is defined as the difference of the ATMD's relative velocity and absolute acceleration of the structural j^{th}-floor on which the ATMD is installed. The PCA-ATMD therefore only uses local measurements from the floor on which the ATMD is located.

The trajectory error can be reduced by negative feedback, so the control force proportional to the trajectory error is designed as

$$u[k] = G_a e_a[k] = G_a \boldsymbol{d}_{rv}\boldsymbol{z}[k] + G_a g_a y_f[k] \tag{12}$$

By substituting Eqs. (10)-(11) into Eq. (12), the ATMD phase control force is then designed as

$$u[k] = \frac{G_a \boldsymbol{d}_{rv} + G_a g_a \boldsymbol{C}}{(1 - G_a g_a D)}\boldsymbol{z}[k] = \boldsymbol{G}\boldsymbol{V}\boldsymbol{z}[k] \tag{13}$$

where $\boldsymbol{G} = \left[\frac{G_a}{(1-G_a g_a D)} \quad \frac{G_a g_a}{(1-G_a g_a D)}\right]$ is the gain matrix for the structural absolute-acceleration-feedback phase control force; G_a and g_a are the gain parameters of the phase control force that should also be optimized; and $\boldsymbol{V} = \begin{bmatrix}\boldsymbol{d}_{rv} \\ \boldsymbol{C}\end{bmatrix}$ is the corresponding output matrix.

In Eq. (13), if the gain matrix **G** is optimized, then the gain parameter G_a and amplitude ratio g_a can also be optimally determined. However, because the desired phase control force, $u(t)$, is designed as proportional to the system complete state $\mathbf{z}[k]$ and not using full-state feedback, the traditional LQR method cannot be applied to optimize gain matrix **G**. The optimal gain matrix $\boldsymbol{G} = \left[\frac{G_a}{1-G_a g_a D} \quad \frac{G_a g_a}{1-G_a g_a D}\right]$ can, however, be calculated using the discrete-time direct output feedback (Lin *et al*. 1996) such that the performance index

$$J = \sum_{k=0}^{\infty}(\boldsymbol{z}^T[k]\boldsymbol{Q}\boldsymbol{z}[k] + u^T[k]\boldsymbol{R}u[k]) \tag{14}$$

is minimized subject to the constraints of Eq. (4). In Eq. (14), **Q** is the positive semi-definite weighting matrix for the system states and **R** is the positive definite weighting scalar of the control force. The detailed derivation of the direct output-feedback optimization of the discrete-time system is shown in the Appendix. It is worth remarking that the direct output-feedback method ensures the optimal control gain will always stabilize the controlled system, and so the stability of the active control system is ensured.

Thus, after the gain matrix, $\boldsymbol{G} = \left[\frac{G_a}{1-G_a g_a D} \quad \frac{G_a g_a}{1-G_a g_a D}\right] = [G_1 \quad G_2]$, has been optimized using the direct output-feedback method, the optimal design of the gain parameter, G_a, and amplitude ratio, g_a, of the PCA-ATMD can then be obtained as

$$G_a = \frac{G_1}{1+G_2 \boldsymbol{d}_{sa}\boldsymbol{B}_s}, \text{ and } g_a = \frac{G_2}{G_1} \tag{15}$$

Therefore, the real-time active control force of the PCA-ATMD is obtained using only the ATMD's velocity relative to the structure and the filtered absolute acceleration of the structural floor, as shown in Eq. (13). The control flow chart is shown in Fig. 3.

4. Experimental setup

A steel MDOF shear building with an ATMD was considered to demonstrate the control performance of the proposed PCA-ATMD.

4.1 3-DOF building structure

The three-story shear building specimen shown in Fig. 4 was used as a 3-DOF benchmark structure. The length and width of the floor plan of the building were approximately 800 mm and 300 mm, respectively. The clear height of the building was approximately 330 mm and each floor was installed with six columns fastened by bolts. To emphasize the higher-mode behavior of the structure, the mass and stiffness of the building were specifically designated. The floor masses of the 1st, 2nd, and top floor were set at 16.97 kg, 12.95 kg, and 33.93 kg, respectively. The stiffnesses of the 1st, 2nd, and 3rd floor were set at 24,231.9 N/m, 7013.6 N/m and 7455.8 N/m, respectively. The natural frequencies of the 1st, 2nd, and 3rd mode were 1.429 Hz, 5.054 Hz, and

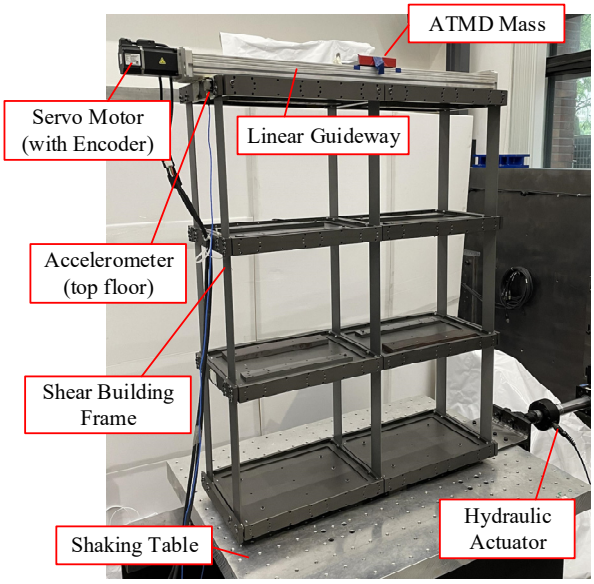

Fig. 4 Configuration of the experimental building structure specimen

Table 1 3-DOF shear building structure parameters

	1st floor	2nd floor	3rd floor (top)
Floor mass (kg)	16.97	12.95	33.93
Story stiffness (N/m)	24231.9	7013.6	7455.8
	1st mode	2nd mode	3rd mode
Modal frequency (Hz)	1.429	5.054	7.273
Modal damping ratio (%)	0.3	0.3	0.3
Modal mass participation ratio (%)	79.0	11.3	9.7

7.273 Hz, respectively and the effective masses as a percentage of the total mass of each mode were 79.0%, 11.3% and 9.7%. The participation percentage of the first mode was less than 80% and that of the second mode was higher than 10%, and the higher a mode, the more its contribution is considered to approach skyscraper behavior. The modal damping for each mode was approximately 0.3% as measured in the system identification experiment. The 3-DOF structure parameters are listed in Table 1.

The 3-DOF shear building was installed on a uniaxial shaking table in a small-scale structural laboratory located in the National Center for Research on Earthquake Engineering (NCREE) in Taipei, Taiwan. The uniaxial shaking table was actuated by a hydraulic actuator with a force and stroke capacity of 15 kN and ±127 mm (Chen *et al*. 2020), respectively, to excite the building in the long direction of the floor plan view shown in Fig. 4.

4.2 Active tuned mass damper system and control/measurement units

A single-axis motor-driven ball-screw linear guider was used in the ATMD system and installed at the top of the 3-DOF building (Fig. 4). The motor-driven linear guider

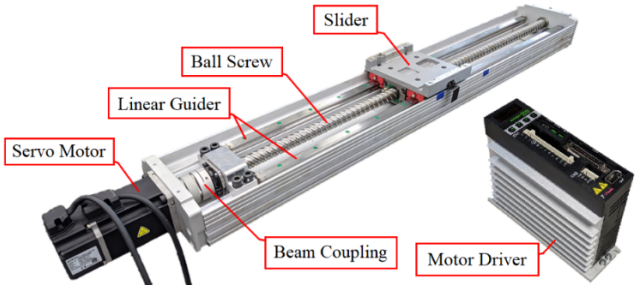

Fig. 5 Photograph of the motor-driven ball-screw linear guider and driver (Lai *et al*. 2022)

Table 2 ATMD system parameters

ATMD mass ratio (%)	3.54
ATMD mass (kg)	1.40
ATMD inertial mass (kg)	3.73
ATMD virtual stiffness (N/m)	413.865
ATMD virtual damping coefficient (N-s/m)	18.436
ATMD frequency ratio	1.0
ATMD damping ratio	0.2

consisted of a moving slider, a ball-screw guider, and an AC-driven motor to provide the control forces, as shown in Fig. 5. The ATMD parameters are listed in Table 2. The mass of the moving slider, md, was 1.40 kg (Table 2). The inertial mass, mi, of all rotating elements including the ball-screw shaft, beam coupling, and rotator was 3.73 kg (Table 2). In addition, the motor-driven linear guider is without a physical spring or damping to generate the restoring force and damping force of the moving slider mass. The restoring force can be directly replaced by the motor-driven force which is determined by multiplication of the displacement of slider and the virtual stiffness. The virtual stiffness has the same function as k_d which is designed as 413.865 (N/m) so that the ATMD is tuned to the first modal frequency of the 3-DOF structure with a frequency ratio of 1.0 (Table 2). Meanwhile, the damping force is also generated by the motor-driven force by multiplication of the velocity of slider and an assigned ATMD damping coefficient of 18.436 (Table 2).

The masses of the stationary components of the linear guider were included in the top floor mass (Table 1). The lead and diameter of the ball-screw shaft were 40 mm and 20 mm, respectively. The motor was directly connected to the ball-screw shaft by a beam coupling. The AC servo-motor (FRMS4B20606A) had a rated power of 400W and was driven by a servo motor driver (D2T-0423-S-B4) (Fig. 5) in the servo-velocity control mode.

To demonstrate the application of the PCA-ATMD, a Micro-Box 2000 x86 based controller with an embedded Sensoray 526 AD/DA converter with encoder input (Fig. 6(a)) developed by TeraSoft Inc. was adopted for a real-time control prototype under the xPC target model. After the control flow diagrams were built in a Matlab/Simulink environment on a host PC, the executable C-codes were

compiled and downloaded into a target PC (Micro-Box 2000) to execute real-time control. Low-cost and high-resolution MEMS accelerometers (3711E112G) (Fig. 6(b)) manufactured by PCB Group Inc. that have a measurement range of ±2 g for single-end signal output were installed on the top of the shear building structure for the control application. An incremental encoder with the high resolution of 131,072 counts/rev was embedded in the AC servo motor to measure motor rotation so that the ATMD stroke could be determined. The relative velocity of the ATMD could then be derived from the ATMD stroke. The hardware layout for the experimental verification is shown in Fig. 7.

From the experiment layout, it is evident that all measurement and control units can be located on the same floor where the PCA-ATMD is installed. Consequently, the PCA-ATMD is highly compact and can be apply in a decentralized manner. These aspects highlight the convenient of utilizing and maintaining the PCA-ATMD in high-rise buildings.

4.3 Servo-velocity control of the ATMD system

In order to reduce the loss of the applied phase-control force due to undesired friction, the servo-velocity control mode was adopted to drive the ATMD. However, the active phase control law captures the required phase control force $u(t)$ but not the reference velocity. At this stage, the structural disturbance rejection problem becomes a reference tracking problem. Therefore, the real-time reference velocity predictor of the ATMD has to be established. The equation of motion of the only ATMD system is taken from Eq. (2) and recast in relative coordinates

$$(m_d + m_i)[\ddot{x}_d(t) - \ddot{x}_j(t)] + c_d[\dot{x}_d(t) - \dot{x}_j(t)] + k_d[x_d(t) - x_j(t)] = -u(t) - m_d\{\ddot{x}_j(t) + \ddot{x}_g(t)\} \quad (16)$$

where $\{\ddot{x}_j(t) + \ddot{x}_g(t)\} = \ddot{x}_j^t(t)$ is the absolute acceleration of the structural floor on which the ATMD is located. The ATMD system is then treated as an SDOF system excited by the absolute acceleration of structural floor and active control force. The state-space representation of Eq. (16) is expressed as

$$\dot{\bar{\boldsymbol{z}}}(t) = \bar{\boldsymbol{A}}\bar{\boldsymbol{z}}(t) + \bar{\boldsymbol{B}}u(t) + \bar{\boldsymbol{E}}\{\ddot{x}_j(t) + \ddot{x}_g(t)\} \quad (17)$$

where $\bar{\boldsymbol{z}}(t) = \begin{bmatrix} x_d(t) - x_j(t) \\ \dot{x}_d(t) - \dot{x}_j(t) \end{bmatrix}$ is a state vector of the ATMD system in relative coordinates; the system matrix of the ATMD system $\bar{\boldsymbol{A}} = \begin{bmatrix} 0 & 1 \\ -(m_d + m_i)^{-1}k_d & -(m_d + m_i)^{-1}c_d \end{bmatrix}$; the control force location vector $\bar{\boldsymbol{B}} = \begin{bmatrix} 0 \\ -(m_d + m_i)^{-1} \end{bmatrix}$; and the excitation location vector $\bar{\boldsymbol{E}} = \begin{bmatrix} 0 \\ -(m_d + m_i)^{-1}m_d \end{bmatrix}$. The discrete-time state-space equation can be derived as

$$\bar{\boldsymbol{z}}[k+1] = \bar{\boldsymbol{A}}_d\bar{\boldsymbol{z}}[k] + \bar{\boldsymbol{B}}_d u[k] + \bar{\boldsymbol{E}}_d\{\ddot{x}_j[k] + \ddot{x}_g[k]\} \quad (18)$$

where $\bar{\boldsymbol{A}}_d = e^{\bar{\boldsymbol{A}}\Delta t}$, $\bar{\boldsymbol{B}}_d = \bar{\boldsymbol{A}}^{-1}(\bar{\boldsymbol{A}}_d - \boldsymbol{I})\bar{\boldsymbol{B}}$, and $\bar{\boldsymbol{E}}_d = \bar{\boldsymbol{A}}^{-1}(\bar{\boldsymbol{A}}_d - \boldsymbol{I})\bar{\boldsymbol{E}}$ are the state-space system matrix, control force location vector, and excitation location vector, respectively, in discrete-time sense. Eq. (18) can be seen as a simple one-step predictor where the system matrix and location vectors are determined only by the ATMD parameters and without requiring any structural information. Therefore, this one-step predictor is still valid even when the main structure exhibits non-linear behavior.

Utilizing the absolute acceleration of structural floor, ATMD stroke, and calculated phase control force, the one-step-ahead ATMD velocity can be obtained and extracted from Eq. (18). This predicted ATMD velocity is the reference velocity that can be fed to the motor driver to execute servo-velocity control via the incorporated PD controller established and tuned for the motor in advance. Furthermore, the ATMD stroke can also be used as a corrector to replace the predicted ATMD stroke in Eq. (18) to ensure the accuracy of the predictor. The flowchart for the reference velocity predictor is shown in Fig. 8.

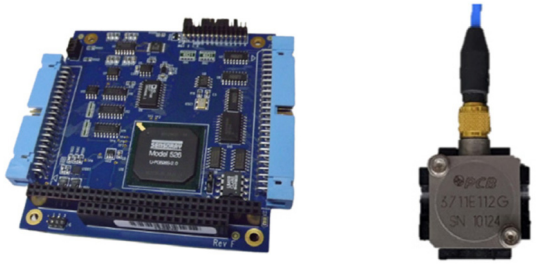

(a) Sensoray 526 AD/DA converter

(b) PCB accelerometer (±2 g)

Fig. 6 Experimental setups

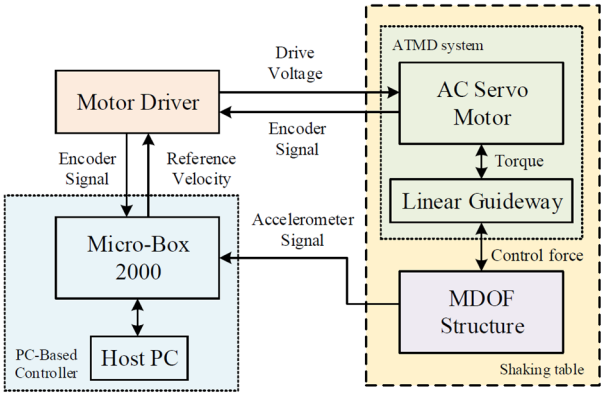

Fig. 7 Hardware layout for experimental verification

4.4 Digital filter for accelerometer signals

The accelerometer is used to measure the absolute acceleration response of the top floor of the structure. However, the environmental noise and friction-induced vibration in acceleration signals generated by the linear guider is of a magnitude of approximately ±0.1 m/s^2. Therefore, a seven-order infinite impulse response (IIR)

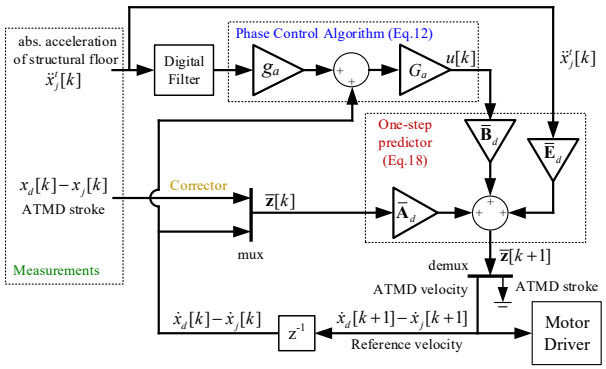

Fig. 8 Flowchart for the reference velocity predictor

band-pass digital filter was adopted to implement real-time filtering to remove noise.

The band-pass digital filter was carefully designed to reduce the high-frequency noise. Moreover, the phase delay caused by the filter was compensated for, especially at the first modal frequency (1.429 Hz), with approximate 0 rad and 2π rad phase shifts for the second modal frequency (5.054 Hz), so that the filter would not significantly distort the acceleration signal. The Bode plots of the IIR filter are shown in Fig. 9 and the coefficients of the designed IIR filter are listed in Table 3.

It is worth mentioning that it is quite simple to design a real-time digital filter for a sensor. However, an applied digital filter will unavoidably distort signals, which might cause instability in the feedback control system even though the digital filter remains stable itself. This issue can be fully avoided in the PCA-ATMD optimal design process by using the complete model. This is because if an inappropriate digital filter is chosen, the discrete-time direct output feedback will no longer be a stable gain matrix solution. At this point, the designer could then redesign the digital filter until a stable gain matrix is obtained by direct output feedback.

Table 3 Coefficients of the seven-order IIR filter

Coefficient	Numerator	Coefficient	Denominator
b_0	1.767198×10^{-7}	a_0	1.000000
b_1	5.301594×10^{-7}	a_1	−6.794844
b_2	1.767198×10^{-7}	a_2	19.812944
b_3	-8.835990×10^{-7}	a_3	−32.137241
b_4	-8.835990×10^{-7}	a_4	31.316814
b_5	1.767198×10^{-7}	a_5	−18.333758
b_6	5.301594×10^{-7}	a_6	5.970382

4.5 Optimal control gains of the PCA-ATMD and numerical assessment

To minimize the total structural strain energy and kinetic energy (the total energy) of the structure, the design weighting of $\boldsymbol{Q}=\begin{bmatrix}0 & \cdots & 0 & \mathbf{0} & \mathbf{0}\\ \vdots & 0.5\boldsymbol{k}_s & \mathbf{0} & \vdots & \\ 0 & \mathbf{0} & 0 & \mathbf{0} & \vdots \\ \mathbf{0} & \cdots & \mathbf{0} & 0.5\boldsymbol{m}_s & \\ \mathbf{0} & & \cdots & & \mathbf{0}_{7\times7}\end{bmatrix}$, $R=1.5\times10^{-4}$, and the initial quartic state $\boldsymbol{Z}_0=\boldsymbol{E}^T\boldsymbol{E}$ were assigned to determine the optimal control gains for the active phase control force, $u(t)$. After the discrete-time direct output-feedback optimization procedure was conducted, as shown in the Appendix, the optimal control gains of the structural absolute acceleration feedback, G_a^{opt} and g_a^{opt}, were calculated as 420.7233 and 0.9026, respectively.

In this section, the performance of the optimally designed PCA-ATMD is numerically investigated in the frequency domain. The frequency response functions for the cases of (1) the 3-DOF structure without using ATMD (uncontrolled), (2) the structure with the PCA-ATMD, and (3) the structure in which the full-state feedback conventional LQR-ATMDs were individually simulated when subjected to ground acceleration. Notice that conventional LQR-ATMD was designed using full-state feedback and the control force was adjusted so that the H2 norms of the structural responses are identical with the PCA-ATMD for comparison. The frequency response functions of the structural displacement and the absolute acceleration are shown in Figs. 10 and 11, respectively.

In Figs. 10 and 11, the response curves show that the PCA-ATMD significantly suppresses the peaks as well as the H2 norms for both the structural displacement and absolute acceleration responses, especially the structural response for the first mode (1.429 Hz) and second mode (5.054 Hz). In addition, the peak performance of the PCA-ATMD was similar to that of the LQR-ATMD but it required far fewer measurements. Therefore, the PCA-ATMD is more feasible than conventional LQR-ATMD for application in building structures. Moreover, the PC-ATMD phase relative to the structure is shown in Fig. 12. As shown

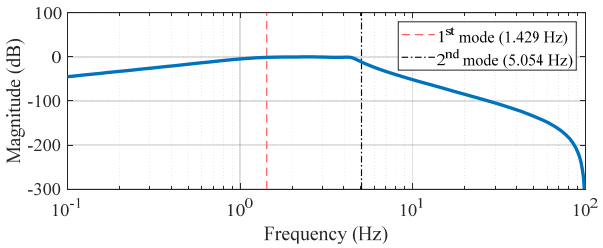

(a) Magnitude

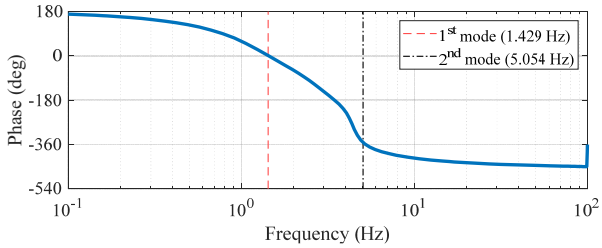

(b) Phase

Fig. 9 Bode plots of the designed IIR filter

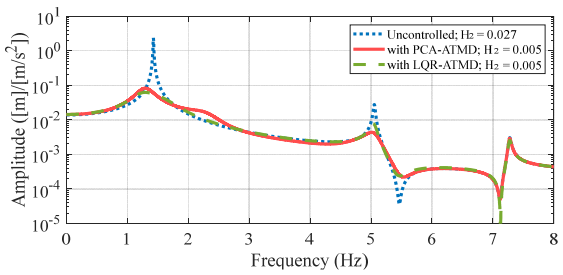

Fig. 10 Frequency response functions of structural displacement

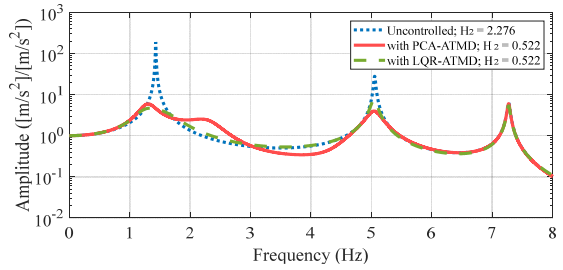

Fig. 11 Frequency response functions of absolute acceleration of structure

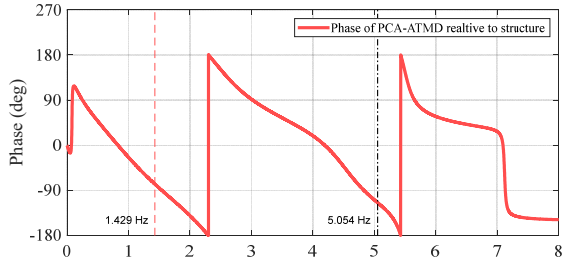

Fig. 12 Frequency response functions of PCA-ATMD phase relative to structure

in Fig. 12, the phase of PCA-ATMD relative to the structure at first mode (1.429 Hz) is very close to -90 degrees. This demonstrates that the PCA-ATMD exhibits maximum power flow and possesses significant vibration reduction capabilities.

Although the direct output-feedback algorithm ensures a stable optimal control gain for the controlled system, the stable gain range of the PCA-ATMD was still investigated before the experiment. All of the eigenvalues of the discrete-time state-space system matrix, $[\boldsymbol{A}+\boldsymbol{BGV}]$, must fall within the unit circle on the complex plane to guarantee the stability of the control system. To verify the stable range of the control system, the control gain parameters were varied over a certain range. Fig. 13 illustrates the stable range of control gain G_a, which was varied from 0% to 480% of the optimal value for which g_a does not vary. Fig. 14 illustrates the stable range of the control gain g_a, which varies from 0% to 150% of the optimal value for which G_a does not vary.

As seen in Figs. 13 and 14, when the control gain falls within those ranges, the resulting eigenvalues are all within the unit circle on the complex plane. The PCA-ATMD can

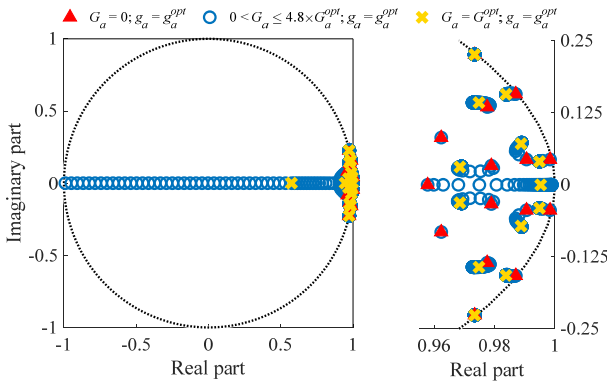

Fig. 13 Stability analysis of the stable range of the gain parameter G_a

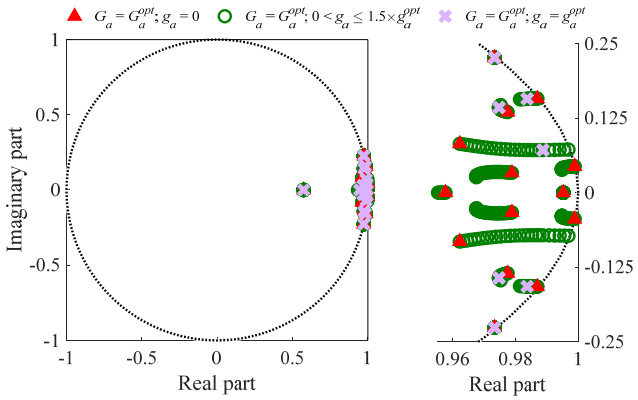

Fig. 14 Stability analysis of the stable range of the amplitude ratio g_a

operate within a certain (large) gain range to maintain stability, which demonstrates the robustness of the proposed control algorithm.

5. Experimental verification

5.1 Demonstration of servo-velocity control

In order to verify whether the servo-velocity-controlled motor-driven ball-screw linear guider produces the expected ATMD behavior, the time histories of the reference velocity and measured velocity of the linear guider are illustrated in Fig. 15(a) as well as their difference in Fig. 15(b).

As shown in Fig. 15(a), most of the time the motor-driven linear guider performs well at tracking the reference velocity, especially when the effect of friction is sufficiently reduced. The maximum difference between the reference velocity and measured velocity is 0.010 m/s, as shown in Fig. 15(b). The measured velocity only differs to a large degree when the value of the reference velocity is small and close to zero. Furthermore, the response time of the AC-motor was extremely fast and the time delay of the first command was almost within one-time step, i.e., 0.005 s. The time delay issue can be neglected in this experiment, as shown in Fig. 15.

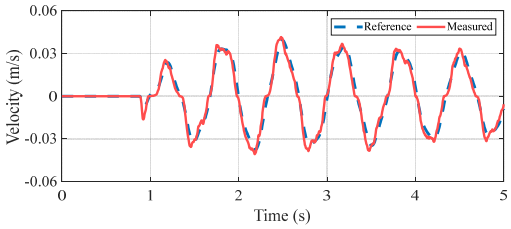

(a) The reference velocity and measured velocity

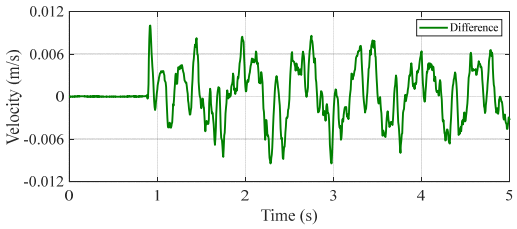

(b) The tracking difference

Fig. 15 Time histories of the reference velocity, measured velocity and the tracking difference

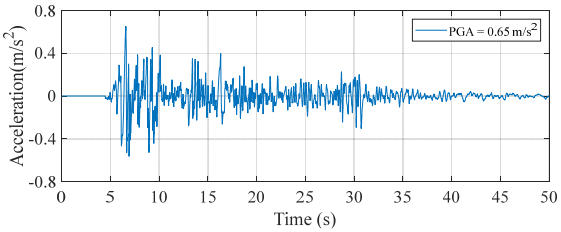

Fig. 16 El Centro earthquake records (scaled)

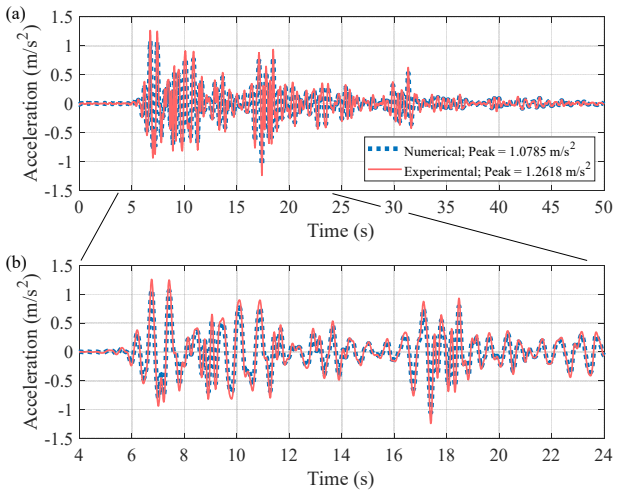

Fig. 17 Comparison of the numerical and experimental results of the absolute acceleration of the roof: (a) time history and (b) the first 4.0 to 24.0 s

5.2 Verification of the seismic time-history numerical simulation and experimental results

To verify that the proposed PCA-ATMD behavior was as expected, a comparison of the numerical and experimental results was conducted. The numerical time-history results were obtained using a state-space method to calculate the MDOF structure and PCA-ATMD responses. Under the El Centro earthquake with a scaled PGA of 65 gal, as shown in Fig. 16, the corresponding time histories of the numerical simulation and experimental results are shown in Figs. 17 and 18.

The time history of the absolute acceleration of the roof is shown in Fig. 17(a) and the first 10.0 to 25.0 s of significant reaction are shown in Fig. 17(b). Fig. 17 shows that the time history of the roof's acceleration is quite comparable, with the peak responses differing by only approximately 17.0%. In addition, the peak responses of the ATMD stroke differed by only approximately 3.3%, as shown in Fig. 18(a), and the peak responses of the active control force differed by only approximately 3.3%, as shown in Fig. 18(b). These comparison results demonstrate that the PCA-ATMD behavior and performance are fairly predictable.

5.3 Evaluation of PCA-ATMD performance

Six additional ground accelerations were used to investigate the PCA-ATMD performance for suppression of structural vibration. These scaled ground accelerations had different seismic site effects (Semblat and Pecker 2009), including far-field, near-fault, and basin effects as listed in Table 4.

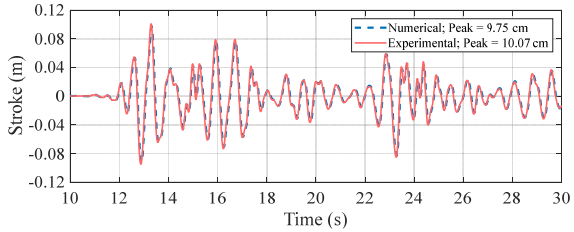

(a) PCA-ATMD stroke

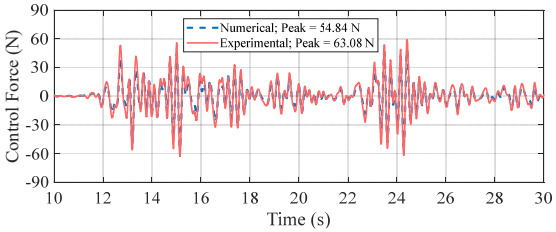

(b) Active control force

Fig. 18 Comparison of numerical and experimental results of PCA-ATMD stroke and active control force

Table 4 Ground acceleration records for the experimental validation test

Year	Earthquake record	Scaled PGA (gal)	Site effect
1940	El Centro	65	Far-field
1995	JMA Kobe	55	Near-fault
1999	Chi-Chi TAP100	60	Basin and far-field
2016	JMA Kumamoto	60	Near-fault
2016	Meinong TCU109	150	Far-field
2018	Hualien HWA048	100	Near-fault
2018	Hualien TAP020	35	Basin and far-field

To evaluate the PCA-ATMD performance, the peak acceleration (L_1 norm) reduction ratio is defined as

$$R_{L1} = \left[1 - \frac{\max(|\ddot{x}_3^t|)_{\text{with control}}}{\max(|\ddot{x}_3^t|)_{\text{w/o control}}}\right] \times 100\% \tag{19}$$

and the root-mean-square (RMS) acceleration (L_2 norm) reduction ratio is defined as

$$R_{L2} = \left[1 - \frac{(\|\ddot{x}_3^t\|_2)_{\text{with control}}}{(\|\ddot{x}_3^t\|_2)_{\text{w/o control}}}\right] \times 100\% \tag{20}$$

where $\ddot{x}_3^t = \ddot{x}_3(t) + \ddot{x}_g(t)$ is the absolute acceleration of the top floor of the 3-DOF shear frame. The higher the

Table 5 Structural roof responses and reduction ratios from the experimental validation

	w/o control	with PCA-ATMD			
	Peak absolute acceleration (m/s^2)	Peak absolute acceleration (m/s^2)	Stroke (cm)	R_{L1} (%)	R_{L2} (%)
El Centro	3.770	1.262	10.07	66.5	80.1
Kobe	3.573	1.247	9.61	65.1	86.2
TAP100	3.307	2.045	14.09	38.2	80.2
Kumamoto	2.358	1.716	13.16	27.2	80.7
TCU109	2.623	2.191	14.69	16.5	72.7
HWA048	3.107	1.868	21.85	39.9	67.9
TAP020	3.184	1.001	8.16	68.6	76.2
Average				4.60	77.7

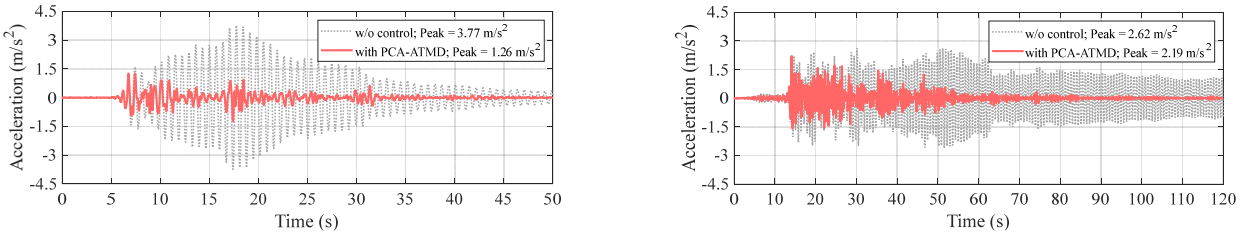

(a) El Centro earthquake (b) TCU109 earthquake

Fig. 19 Time histories of the structural roof acceleration from the experimental validation

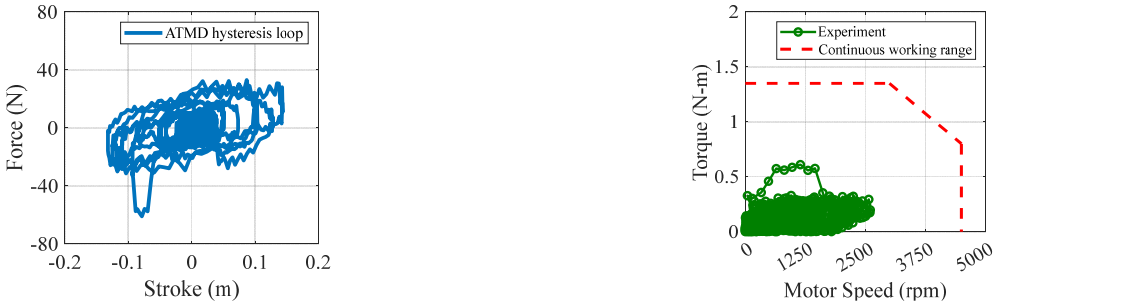

(a) PCA-ATMD hysteresis loop (b) Servo-motor performance curve

Fig. 20 Experimental validation of PCA-ATMD hysteresis loop and servo-motor performance curve

reduction ratio, the better the control performance.

Table 5 shows the experimental results for the control performance with respect to structural peak absolute acceleration and the L_2 norm. From Table 5, it is found by comparison with the uncontrolled case that the PCA-TMD has a strong ability to reduce structural vibration. The average peak absolute acceleration reduction ratio was 46.0% and the worst case was 16.5%. The average RMS acceleration reduction ratio was 77.7% and the worst case was still 67.9%. Furthermore, the experimental results show that site effects do not obviously influence the PCA-ATMD performance, whereas passive TMD is usually discouraged for use with short-duration, pulse-like, near-fault ground motions. The PCA-ATMD, on the other hand, can react swiftly and accurately to suppress the structural responses.

Fig. 19 presents the time histories of the structural response of the 3-DOF structure subjected to the ground accelerations of the El Centro earthquake and TCU109 earthquake. The results shown in Figs. 19(a)-(b) show that the PCA-ATMD can suppress the structural absolute acceleration response. Although the peak absolute acceleration reduction ratio under the TCU109 earthquake ground accelerations shown in Fig. 19(b) are not as good as under the El Centro earthquake accelerations shown in Fig. 19(a), the effect on the resilience of the structural responses by the PCA-ATMD is clearly remarkable.

The servo motor driver continuously monitors the AC-motor RMS current, which can be used to estimate the generated torque. Therefore, the applied servo control force of the PCA-ATMD can be obtained. Fig. 20 depicts the PCA-ATMD hysteresis loop and servo-motor performance curve for the case of the HWA048 earthquake. It is worth noting that, in Fig. 20(a), the servo control force includes not only the active control force and the virtual restoring force of the PCA-ATMD but also the friction compensated force that is automatically compensated for by the servo-velocity control. Fig. 20(b) shows the motor performance curve. Neither the motor rotational speed nor the torque are beyond the motor's working range, which complies with the operational requirements for motor capacity.

6. Conclusions

In this paper, numerical simulation analysis and shaking table experiments were conducted for a phase-control absolute-acceleration-feedback active tuned mass damper (PCA-ATMD) incorporated into a multiple-degree-of-freedom (MDOF) building structure. The feasibility and efficacy of the PCA-ATMD for structural vibration mitigation were demonstrated and verified. The complete system combining the MDOF structure with the PCA-ATMD and a real-time filter was derived in state-space form so that the physical meaning of the states of the combined system could be well-determined. The PCA-ATMD was optimized using the discrete-time direct output-feedback method. By applying direct output feedback to the combined system, not only were the gain parameters of the PCA-ATMD optimized but also the instability of the active control system was prevented. When operating the PCA-ATMD, only the relative velocity (or stroke) of the ATMD relative to the structure and the absolute acceleration of the building floor on which the PCA-ATMD is located needs to be measured. The phase control algorithm is decentralized and all of the required measurements are from the floor on which the PCA-ATMD is installed. Neither full-state feedback nor estimation is required.

Numerical simulation conducted on a three-story shear building showed that the performance of the PCA-ATMD is comparable to that of a conventional LQR-ATMD. The PCA-ATMD exhibits a phase angel of 90 degrees lag of the structure at the first mode, indicating its significant vibration reduction capabilities. Experimental results for the MDOF building subjected to seven earthquake ground accelerations showed that the PCA-ATMD system is quite effective at mitigating the structural vibration of both the peak and RMS responses, with average reduction ratios of 46.0% and 77.7%, respectively. By the proposed reference velocity predictor, the servo-velocity-controlled technology for ATMD system is developed. The servo-velocity-controlled PCA-ATMD was found to be able to react swiftly and accurately to suppress structural responses and the simulation and experimental results showed great consistency. Furthermore, the experimental results also indicated that site effects did not significantly influence PCA-ATMD performance.

Acknowledgments

This research was financially supported by the Natural Science and Technology Council (NSTC) of Taiwan under Grant No. MOST 109-2222-E-008 -001 -MY2.

References

Allaoua, S. and Guenfaf, L. (2019), "LQG vibration control effectiveness of an electric active mass damper considering soil–structure interaction", *Int. J. Dyn. Control*, **7**, 185-200. https://doi.org/10.1007/s40435-018-0428-9

Amini, F., Tourani, N. and Ghaderi, P. (2018), "Performance evaluation of phase-controlled semiactive resettable TMD (PCRTMD) with the stiffness retuning ability under strong seismic motions", *Struct. Des. Tall Special Build.*, **27**(16), e1502. https://doi.org/10.1002/tal.1502

Aydin, E., Ozturk, B. and Dutkiewicz, M. (2019), "Analysis of efficiency of passive dampers in multistorey buildings", *J. Sound Vib.*, **439**(20), 17-28. https://doi.org/10.1016/j.jsv.2018.09.031

Ayorinde, E.O. and Warburton, G.B. (1980), "Minimizing structural vibrations with absorbers", *Earthq. Eng. Struct. Dyn.*, **8**, 219-236. https://doi.org/10.1002/eqe.4290080303

Bakre, S.V. and Jangid, R.S. (2007), "Optimum parameters of tuned mass damper for damped main system", *Struct. Control Health Monitor.*, **14**, 448-470. https://doi.org/10.1002/stc.166

Casciati, F., Rodellar, J. and Yildirim, U. (2012), "Active and semi-active control of structures–theory and applications: A review of recent advances", *J. Intell. Mater. Syst. Struct.*, **23**(11), 1181-1195. https://doi.org/10.1177/1045389X12445029

Chang, J.C.H. and Soong, T.T. (1980), "Structural control using active tuned mass dampers", *J. Eng. Mech.*, **106**, 1091-1098. https://doi.org/10.1061/JMCEA3.0002652

Chang, C.C. and Yang, H.T.Y. (1995), "Control of buildings using active tuned mass dampers", *J. Eng. Mech.*, **121**, 355-366.

https://doi.org/10.1061/(ASCE)0733-9399(1995)121:3(355)
Chen, P.C, Ting, G.C. and Li, C.H. (2020), "A versatile small-scale structural laboratory for novel experimental earthquake engineering", *Earthq. Struct., Int. J.*, **18**(3), 337-348. https://doi.org/10.12989/eas.2020.18.3.337
Chen, P.C., Sugiarto, B.J. and Chien, K.Y. (2021), "Performance-based optimization of LQR for active mass damper using symbiotic organisms search", *Smart Struct. Syst., Int. J.*, **27**(4), 705-717. https://doi.org/10.12989/sss.2021.27.4.705
Chu, S.Y., Soong, T.T. and Reinhorn, A.M. (2005), *Active, Hybrid, and Semi-active Structural Control: A Design and Implementation Handbook*, Wiley, New York, USA.
Chung, L.L., Lin, R.C., Soong, T.T. and Reinhorn, A.M. (1989), "Experimental study of active control for MDOF seismic structures", *J. Eng. Mech.*, **115**, 1609-1627. https://doi.org/10.1061/(ASCE)0733-9399(1989)115:8(1609)
Chung, L.L., Lai, Y.A., Yang, C.S.W., Lien, K.H. and Wu, L.Y. (2013), "Semi-active tuned mass dampers with phase control", *J. Sound Vib.*, **332**, 3610-3625. https://doi.org/10.1016/j.jsv.2013.02.008
Concha, A., Thenozhi, S., Betancourt, R.J. and Gadi, S.K. (2021), "A tuning algorithm for a sliding mode controller of buildings with ATMD", *Mech. Syst. Signal Process.*, **154**(1), 107539. https://doi.org/10.1016/j.ymssp.2020.107539
Dai, J., Xu, Z.D., Gai, P.P. and Li, H.W. (2020), "Effect of frequency dependence of large mass ratio viscoelastic tuned mass damper on seismic performance of structures", *Soil Dyn. Earthq. Eng.*, **130**, 105998. https://doi.org/10.1016/j.soildyn.2019.105998
Den Hartog, J.P. (1956), *Mechanical Vibrations*, McGraw-Hill, New York, USA.
Ferreira, F., Moutinho, C., Cunha, A. and Caetano, E. (2018), "Proposal of optimum tuning of semiactive TMDs used to reduce harmonic vibrations based on phase control strategy", *Struct. Control Health Monitor.*, **25**, e2131. https://doi.org/10.1002/stc.2131
Frahm, H. (1911), *Device for Damping Vibration of Bodies*; US. Patent No. 989958.
Ghosh, A. and Basu, B. (2005), "A closed-form optimal tuning criterion for TMD in damped structures", *Struct. Control Health Monitor.*, **14**, 681-692. https://doi.org/10.1002/stc.176
Guclu, R. and Yazici, H. (2008), "Vibration control of a structure with ATMD against earthquake using fuzzy logic controllers", *J. Sound Vib.*, **318**, 36-49. https://doi.org/10.1016/j.jsv.2008.03.058
Gutierrez Soto, M. and Adeli, H. (2013), "Tuned mass dampers", *Arch. Computat. Methods Eng.*, **20**, 419-431. https://doi.org/10.1007/s11831-013-9091-7
Ikeda, Y. (2009), "Active and semi-active vibration control of buildings in Japan-Practical applications and verification", *Struct. Control Health Monitor.*, **16**, 703-723. https://doi.org/10.1002/stc.315
Kareem, A., Kijewski, T. and Tamura, T. (1999), "Mitigation of motions of tall buildings with specific examples of recent applications", *Wind Struct., Int. J.*, **2**(3), 201-251. https://doi.org/10.12989/was.2020.2.3.201
Lago, A., Trabucco, D. and Wood, A. (2018), *Damping Technologies for Tall Buildings: Theory, Design Guidance and Case Studies*, Butterworth-Heinemann, Oxford, UK.
Lai, Y.A., Chung, L.L., Yang, C.S.W. and Wu, L.Y. (2018), "Semi-active phase control of tuned mass dampers for translational and torsional vibration mitigation of structures", *Struct. Control Health Monitor.*, **25**, e2191. https://doi.org/10.1002/stc.2191
Lai, Y.A., Luo, W.C., Huang, S.K., Yang, C.Y. and Chang, C.M. (2022), "Seismic control of structure with phase control active tuned mass damper", *Struct. Control Health Monitor.*, **29**(7), e2946. https://doi.org/10.1002/stc.2946
Levine, W.S. and Athans, M. (1970), "On the determination of the optimal constant output feedback gains for linear multivariable systems", *IEEE Transact. Automat. Control*, **15**, 44-48. https://doi.org/10.1109/TAC.1970.1099363
Lewis, F.L., Vrabie, D. and Syrmos, V.L. (2012), *Optimal Control*, Wiley, New York, USA.
Li, C. and Liu, Y. (2002), "Active multiple tuned mass dampers for structures under the ground acceleration", *Earthq. Eng. Struct. Dyn.*, **31**, 1041-1052. https://doi.org/10.1002/eqe.136
Li, C., Liu, Y. and Wang, Z. (2003), "Active multiple tuned mass dampers: A new control strategy", *J. Struct. Eng.*, **129**(7), 972-977. https://doi.org/10.1061/(ASCE)0733-9445(2003)129:7(972)
Lin, C.C., Lu, K.H. and Chung, L.L. (1996), "Optimal discrete-time structural control using direct output feedback", *Eng. Struct.*, **18**, 472-480. https://doi.org/10.1016/0141-0296(95)00122-0
Loh, C.H. and Chao, C.H. (1996), "Effectiveness of active tuned mass damper and seismic isolation on vibration control of multi-storey building", *J. Sound Vib.*, **193**(4), 773-792. https://doi.org/10.1006/jsvi.1996.0315
Mitchell, R., Kim, Y., El-Korchi, T. and Cha, Y.J. (2012), "Wavelet-neuro-fuzzy control of hybrid building-active tuned mass damper system under seismic excitations", *J. Vib. Control*, **19**, 1881-1894. https://doi.org/10.1177/1077546312450730
Moerder, D.D. and Calise, A.J. (1985), "Convergence of a numerical algorithm for calculating optimal output feedback gains", *IEEE Transact. Automat. Control*, **30**, 900-903. https://doi.org/10.1109/TAC.1985.1104073
Moutinho, C. (2015), "Testing a simple control law to reduce broadband frequency harmonic vibrations using semi-active tuned mass dampers", *Smart Mater. Struct.*, **24**, 055007. https://doi.org/10.1088/0964-1726/24/5/055007
Murudi, M.M. and Mane, S.M. (2004), "Seismic effectiveness of tuned mass damper (TMD) for different ground motion parameters", In: *World Conference on Earthquake Engineering*, Vancouver, B.C., Canada, Paper No. 2325.
Nagarajaiah, S. (2009), "Adaptive passive, semiactive, smart tuned mass dampers: identification and control using empirical mode decomposition, hilbert transform, and short-term fourier transform", *Struct. Control Health Monitor.*, **16**(7-8), 800-841. https://doi.org/10.1002/stc.349
Nagishima, I. (2001), "Optimal displacement feedback control law for active tuned mass damper", *Earthq. Eng. Struct. Dyn.*, **30**, 1221-1242. https://doi.org/10.1002/eqe.60
Nishimura, I., Kobori, T., Sakamoto, M., Koshika, N., Sasaki, K. and Ohrui, S. (1992), "Active tuned mass damper", *Smart Mater. Struct.*, **1**, 306-311. https://doi.org/10.1088/0964-1726/1/4/005
Paul, S. and Yu, W. (2018), "A method for bidirectional active control of structures", *J. Vib. Control*, **24**(15), 3400-3417. https://doi.org/10.1177/1077546317705556
Pinkaew, T., Lukkunaprasit, P. and Chatupote, P. (2003), "Seismic effectiveness of tuned mass dampers for damage reduction of structures", *Eng. Struct.*, **25**(1), 39-46. https://doi.org/10.1016/S0141-0296(02)00115-3
Rasouli, S.K. and Yahyai, M. (2002), "Control of response of structures with passive and active tuned mass dampers", *Struct. Des. Tall Build.*, **11**, 1-14. https://doi.org/10.1002/tal.181
Saaed, T.E., Nikolakopoulos, G., Jonasson, J.E. and Hedlund, H. (2013), "A state-of-the-art review of structural control systems", *J. Vib. Control*, **21**, 919-937. https://doi.org/10.1177/1077546313478294
Sadek, F., Mohraz, B., Taylor, A.W. and Chung, R.M. (1997), "A method of estimating the parameters of mass dampers for seismic applications", *Earthq. Eng. Struct. Dyn.*, **26**, 617-635. https://doi.org/10.1002/(SICI)1096-9845(199706)26:6<617::AID-EQE664>3.0.CO;2-Z

Samali, B and Al-Dawod, M. (2003), "Performance of a five-storey benchmark model using an active tuned mass damper and a fuzzy controller", *Eng. Struct.*, **25**, 1597-1610. https://doi.org/10.1016/S0141-0296(03)00132-9

Semblat, J.F., and Pecker, A. (2009), *Waves and Vibrations in Soils*: *Earthquakes*, *Traffic*, *Shocks*, *Construction Works*. IUSS Press, Rome, Italy.

Sone, T., Ogino, K., Kamoshita, N., Muto, K., Ide, Y., Murata, K., Hamaguchi, H. and Yamamoto, M. (2019), "Experimental verification of a tuned mass damper system with two-phase support mechanism", *Japan Architect. Review*, **2**(3), 251-388. https://doi.org/10.1002/2475-8876.12095

Soong, T.T. and Manolis, G.D. (1987), "Active structures", *J. Struct. Eng.*, **113**, 2290-2301. https://doi.org/10.1061/(ASCE)0733-9445(1987)113:11(2290)

Soong, T.T. and Dargush, G.F. (1997), *Passive Energy Dissipation Systems in Structural Engineering*, Wiley, New York, USA.

Spencer, B.F. Jr. and Nagarajaiah, S. (2003), "State of the art of structural control", *J. Struct. Eng.*, **129**, 845-856. https://doi.org/10.1061/(ASCE)0733-9445(2003)129:7(845)

Spencer, B.F. Jr., Suhardjo, J. and Sain, M.K. (1994), "Frequency domain optimal control strategies for aseismic protection", *J. Eng. Mech.*, **120**, 135-158. https://doi.org/10.1061/(ASCE)0733-9399(1994)120:1(135)

Spencer, B.F. Jr., Dyke, S.J. and Deoskar, H.S. (1998), "Benchmark problems in structural control: part I-Active Mass Driver system", *Earthq. Eng. Struct. Dyn.*, **27**(11), 1127-1139. https://doi.org/10.1002/(SICI)1096-9845(1998110)27:11<1127::AID-EQE774>3.0.CO;2-F

Tigli, O.F. (2012), "Optimum vibration absorber (tuned mass damper) design for linear damped systems subjected to random loads", *J. Sound Vib.*, **331**, 3035-3049. https://doi.org/10.1016/j.jsv.2012.02.017

Tsai, H.C. and Lin, G.C. (1993), "Optimum tuned-mass dampers for minimizing steady-state response of support-excited and damped systems", *Earthq. Eng. Struct. Dyn.*, **22**, 957-973. https://doi.org/10.1002/eqe.4290221104

Warburton, G.B. (1982), "Optimum absorber parameters for various combinations of response and excitation parameters", *Earthq. Eng. Struct. Dyn.*, **10**, 381-401. https://doi.org/10.1002/eqe.4290100304

Yang, J.N. (1987), "New optimal control algorithms for structural control", *J. Eng. Mech.*, **113**, 1369-1386. https://doi.org/10.1061/(ASCE)0733-9399(1987)113:9(1369)

Yang, D.H., Shin, J.H., Lee, H.W., Kim, S.K. and Kwak, M.K. (2017), "Active vibration control of structure by active mass damper and multi-modal negative acceleration feedback control algorithm", *J. Sound Vib.*, **392**, 18-30. https://doi.org/10.1016/j.jsv.2016.12.036

Younespour, A. and Ghaffarzadeh, H. (2015), "Structural active vibration control using active mass damper by block pulse functions", *J. Vib. Control*, **21**, 2787-2795. https://doi.org/10.1177/1077546313519285

Appendix

The discrete-time direct output-feedback problem (Lin *et al*. 1996, Lewis *et al*. 2012) solves for the static optimal control gain by directly using measured feedback. The quadratic initial condition is further explained here. A single-input-single-output (SISO) system yields the following equations

$$\begin{aligned} &\boldsymbol{z}[k+1] = \boldsymbol{A_d z}[k] + \boldsymbol{B}_d u[k] + \boldsymbol{E}_d \ddot{x}_g[k] \\ &\boldsymbol{y}[k] = \boldsymbol{V z}[k], \text{and} \\ &u[k] = \boldsymbol{G y}[k] \end{aligned} \tag{A1}$$

where $\mathbf{z}[k]$ is the state and $\mathbf{y}[k]$ is the measurement output. Note that the dimension of measurement, $\mathbf{y}[k]$, is less than the dimension of full-state, $\mathbf{z}[k]$. If the system is subject to impulse excitation from rest, then the system propagation state solution is

$$\boldsymbol{z}[k] = (\boldsymbol{A}_d + \boldsymbol{B}_d \boldsymbol{G V})^k \boldsymbol{z}_0 \tag{A2}$$

where $\boldsymbol{z}_0 = \boldsymbol{E}_d$ is the initial state. To obtain the optimal output-feedback gain, $\mathbf{G}$, the quadratic object function of the above equation is defined as

$$J = \sum_{k=0}^{\infty} \{z^T[k] \boldsymbol{Q} z[k] + u^T[k] R u[k]\} \tag{A3}$$

where $\mathbf{Q}$ is the symmetric positive semi-definite weight matrix and R is the positive definite weight scalar (single-input) of the control force.

Substituting Eqs. (A1) and (A2) into Eq. (A3) yields

$$\begin{aligned} J &= \sum_{k=0}^{\infty} \mathbf{z}_0^T \left\{ \left[(\mathbf{A}_d + \mathbf{B}_d \mathbf{G V})^k \right]^T (\mathbf{Q} + \mathbf{V}^T \mathbf{G}^T R \mathbf{G V}) (\mathbf{A}_d + \mathbf{B}_d \mathbf{G V})^k \right\} \mathbf{z}_0 \\ &\equiv \mathbf{z}_0^T \mathbf{H} \mathbf{z}_0 \end{aligned} \tag{A4}$$

where the constant matrix $\mathbf{H}$ is defined as

$$\begin{aligned} \boldsymbol{H} = \sum_{k=0}^{\infty} \{ &[(\boldsymbol{A_d} + \boldsymbol{B_d G V})^k]^T (\boldsymbol{Q} + \boldsymbol{V}^T \boldsymbol{G}^T R \boldsymbol{G V}) (A_d \\ &+ B_d \boldsymbol{G V})^k \} \end{aligned} \tag{A5}$$

In order to narrow down the solution space within an asymptotically stable condition, the constant matrix $\mathbf{H}$ is first pre-multiplied by $(\boldsymbol{A_d} + \boldsymbol{B_d G V})^T$ and post-multiplied by $(\boldsymbol{A_d} + \boldsymbol{B_d G V})$. Then the product subtracted from itself yields

$$\begin{aligned} &(\boldsymbol{A_d} + \boldsymbol{B_d G V})^T \boldsymbol{H} (\boldsymbol{A_d} + \boldsymbol{B_d G V}) - \boldsymbol{H} = \\ &\lim_{k \to \infty} \{ [(\boldsymbol{A_d} + \boldsymbol{B_d G V})^k]^T (\boldsymbol{Q} + \boldsymbol{V}^T \boldsymbol{G}^T R \boldsymbol{G V}) (\boldsymbol{A_d} \\ &\quad + \boldsymbol{B_d G V})^k \} - (\boldsymbol{Q} + \boldsymbol{V}^T \boldsymbol{G}^T R \boldsymbol{G V}) \end{aligned} \tag{A6}$$

In Eq. (A6), the first term of the right-hand side will vanish because the controlled system $(\boldsymbol{A_d} + \boldsymbol{B_d G V})$ must be stable; i.e., Eq. (A6) becomes

$$\begin{aligned} (\boldsymbol{A_d} + \boldsymbol{B_d G V})^T \boldsymbol{H} (\boldsymbol{A_d} + \boldsymbol{B_d G V}) - \boldsymbol{H} + (\boldsymbol{Q} \\ + \boldsymbol{V}^T \boldsymbol{G}^T R \boldsymbol{G V}) = 0 \end{aligned} \tag{A7}$$

Eq. (A7) is known as the discrete-time Lyapunov equation and becomes the constraint of the object function. Thus, the Lagrangian multiplier is introduced from Eq. (A7) to Eq. (A4) to form a constrained object function

$$\begin{aligned} J' = \mathrm{tr}(\mathbf{H} \mathrm{Z}_0) + \mathrm{tr}\{ &\boldsymbol{L} [(\boldsymbol{A_d} + \boldsymbol{B_d G V})^T \boldsymbol{H} (\boldsymbol{A_d} + \boldsymbol{B_d G V}) \\ &- \boldsymbol{H} + (\boldsymbol{Q} + \boldsymbol{V}^T \boldsymbol{G}^T R \boldsymbol{G V})] \} \end{aligned} \tag{A8}$$

where $\mathrm{tr}\{.\}$ denotes the trace of the matrix; $\mathrm{tr}(\mathbf{z}_0^T \boldsymbol{H} \boldsymbol{z}_0) = \mathrm{tr}(\mathbf{H} \mathrm{Z}_0)$; $Z_0 = \boldsymbol{z}_0 \boldsymbol{z}_0^T = \boldsymbol{E}_d \boldsymbol{E}_d{}^T$ is the quadratic initial condition matrix; and matrix $\mathbf{L}$ is the Lagrange multiplier matrix. The optimization problem is now converted to minimize the constrained object function. The necessary conditions for solving discrete-time output-feedback problems are given by taking partial derivatives of J' with respect to the independent variables $\mathbf{H}$, $\mathbf{L}$, and $\mathbf{G}$ all being equal to zero

$$\begin{aligned} \frac{\partial J'}{\partial \boldsymbol{L}} = &(\boldsymbol{A_d} + \boldsymbol{B_d G V})^T \boldsymbol{H} (\boldsymbol{A_d} + \boldsymbol{B_d G V}) - \boldsymbol{H} \\ &+ (\boldsymbol{Q} + \boldsymbol{V}^T \boldsymbol{G}^T R \boldsymbol{G V}) = \boldsymbol{0} \end{aligned} \tag{A9}$$

$$\frac{\partial J'}{\partial \boldsymbol{H}} = (\boldsymbol{A_d} + \boldsymbol{B_d G V}) \boldsymbol{L} (\boldsymbol{A_d} + \boldsymbol{B_d G V})^T - \boldsymbol{L} + Z_0 = \boldsymbol{0}, \tag{A10}$$

and

$$\frac{\partial J'}{\partial \boldsymbol{G}} = 2 \boldsymbol{B}_d{}^T \boldsymbol{H} (\boldsymbol{A_d} + \boldsymbol{B_d G V}) \boldsymbol{L} \boldsymbol{V}^T + 2 R \boldsymbol{G V L V}^T = \boldsymbol{0} \tag{A11}$$

Eq. (A11) can then be further rearranged as

$$\boldsymbol{G} = -(\boldsymbol{B}_d{}^T \boldsymbol{H} \boldsymbol{B_d} + R)^{-1} \boldsymbol{B}_d{}^T \boldsymbol{H} \boldsymbol{A_d} \boldsymbol{L} \boldsymbol{V}^T (\boldsymbol{V L V}^T)^{-1} \tag{A12}$$

The optimal output-feedback gain $\mathbf{G}$ can then be obtained by solving the simultaneous equations, Eqs. (A9), (A10), and (A12), through an iteration procedure (Levine and Athans 1970, Moerder and Calise 1985).